HHS Public Access

Author manuscript

Nature. Author manuscript; available in PMC 2016 December 03.

Published in final edited form as:

Nature. ; 534(7605): 63–68. doi:10.1038/nature17679.

Activation of NMDA receptors and the mechanism of inhibition by ifenprodil

Nami Tajima[1], **Erkan Karakas**[1], **Timothy Grant**[2], **Noriko Simorowski**[1], **Ruben Diaz-Avalos**[2], **Nikolaus Grigorieff**[2,*], and **Hiro Furukawa**[1,*]

[1]Cold Spring Harbor Laboratory, WM Keck Structural Biology Laboratory, Cold Spring Harbor, NY11724

[2]Janelia Research Campus, Howard Hughes Medical Institute, Ashburn, VA 20147

SUMMARY

The physiology of *N*-Methyl-D-aspartate (NMDA) receptors in mammals is fundamental to brain development and function. NMDA receptors are ionotropic glutamate receptors that function as heterotetramers composed mainly of GluN1 and GluN2 subunits. Activation of NMDA receptors requires binding of neurotransmitter agonists to a ligand-binding domain (LBD) and structural rearrangement of an amino terminal domain (ATD). Recent crystal structures of GluN1/GluN2B NMDA receptors in the presence of agonists and an allosteric inhibitor, ifenprodil, represent the allosterically inhibited state. However, how the ATD and LBD move to activate the NMDA receptor ion channel remains unclear. Here, we combine x-ray crystallography, single-particle electron cryomicroscopy, and electrophysiology to show that, in the absence of ifenprodil, the bi-lobed structure of GluN2 ATD adopts an open-conformation accompanied by rearrangement of the GluN1-GluN2 ATD heterodimeric interface, altering subunit orientation in the ATD and LBD and forming an active receptor conformation that gates the ion channel.

N-Methyl-D-Aspartate (NMDA) receptors are critically involved in brain development and function including learning and memory formation. NMDA receptors belong to the family of ionotropic glutamate receptors (iGluRs), which are glutamate-gated ion channels comprised of three major families, α-amino-3-hydroxy-5-methyl-4-isoxazole propionic acid (AMPA) (GluA1-4), kainate (GluK1-5), and NMDA receptors (GluN1, GluN2A-D, and GluN3A-B)[1].

*Correspondence and requests for material should be addressed to H.F. (furukawa@cshl.edu) and N.G. (grigorieffn@janelia.hhmi.org).

Author Contributions

The authors jointly contributed to project design. NT and HF did x-ray crystallography and electrophysiology. NS purified and characterized antibodies critical for the x-ray crystallographic study. TG, RDA, NG, and HF were involved in structural analysis by cryo-EM. EK expressed and purified proteins for the cryo-EM analysis and conducted model building and refinement of the cryo-EM structures. NT, EK, TG, NG, and HF were involved in manuscript preparation.

The authors declare no competing financial interests.

Author Information

Atomic coordinates and structure factor for the apo-GluN1b-GluN2B ATD is deposited in the Protein Data Bank under the accession code 5B3J. The cryoEM coordinates are deposited under the accession codes 5FXG, 5FXH, 5FXI, 5FXJ, and 5FXK. The cryoEM maps are deposited in the EMDB under accession code EMD-3352, EMD-3353, EMD-3354, EMD-3355, and EMD-3356.

NMDA receptors are obligatory heterotetramers mainly composed of two copies each of the GluN1 and GluN2 subunits, which bind glycine and L-glutamate, respectively. Under physiological conditions, the opening of the NMDA receptor ion channel requires concurrent binding of glycine and L-glutamate[2–4] and relief of magnesium block at the ion channel pore by membrane depolarization[5,6]. The resulting calcium flux[7] triggers a cascade of signal transduction necessary for synaptic plasticity[8]. Dysfunctional NMDA receptors are implicated in various neurological diseases and disorders such as Alzheimer's disease, depression, stroke, epilepsy, and schizophrenia[1,9].

NMDA receptor subunits, like those of other iGluR family members, are composed of multiple domains including an amino terminal domain (ATD), a ligand-binding domain (LBD), a transmembrane domain (TMD), and a carboxy terminal domain (CTD) (Extended Data Fig. 1). Binding of neurotransmitter agonists to the LBD produces a large conformational change involving closure of the bi-lobed structure that is required for ion channel gating in all iGluRs[10–12], but a distinctive feature of NMDA receptors is that activity is also significantly regulated by the ATD[13]. For example, the ATD controls the open probability and speed of deactivation[14,15] and binds allosteric modulator compounds to regulate ion channel activity[16]. In contrast to NMDA receptors, there is no apparent role for the ATDs of AMPA and kainate receptors[17–20] in regulating the ion channel activities even though they are essential for subunit assembly[21]. The recent crystal structures of intact heterotetrameric GluN1/GluN2B NMDA receptors complexed with agonists and allosteric inhibitors, ifenprodil or Ro25-6981, revealed that the ATD and LBD interact tightly via a large interface area, unlike GluA2 AMPA receptor and GluK2 kainate receptor whose ATDs and LBDs minimally interact[17,20,22,23], implying that activation of NMDA receptors requires concerted conformational alterations in the ATD and LBD[19,22,23]. The structures of the intact GluN1/GluN2B NMDA receptors[22,23] and of the isolated ATDs complexed to ifenprodil[24] or zinc[25] showed a closed conformation of the bi-lobed GluN2B ATD architecture[22–25], likely representing the 'allosterically inhibited' functional state. In the presence of agonists, NMDA receptors are known to reside in active states that can trigger ion channel opening, as well as desensitized states with a channel that is closed even in the presence of bound agonists[26]. Despite accumulating structural information on intact NMDA receptors[22,23], as well as isolated ATDs[24,25,27] and LBDs[11,28,29] there is a lack of structures representing the active state and the mechanism of activation has remained unclear. In this study, we present structures of the isolated ATD in the apo-state and of the intact receptor in the activated conformation, providing a detailed mechanistic picture of receptor activation.

Crystal structure of GluN1b-GluN2B ATD in the apo state reveals opening of the bilobed GluN2B ATD and subunit rearrangement compared to the phenylethanolamine-bound structure

The only available structures for the heterodimeric NMDA receptor ATDs to date are those bound to allosteric inhibitors, ifenprodil and Ro25-6981, representing the allosterically inhibited state[22–25]. We reasoned that by conducting structural studies without allosteric inhibitors, we should capture the ATD conformation that can activate the NMDA receptor ion channel. Thus, we obtained the crystal structure of GluN1-GluN2B ATDs in the absence

of an allosteric inhibitor (apo-GluN1b-GluN2B ATD) at 2.9 Å resolution (Extended Data Table 1). This was achieved by crystallizing the purified GluN1b-GluN2B ATD proteins complexed to a Fab fragment derived from mouse monoclonal IgGs to improve the quality of the crystals (Extended Data Fig. 2). The crystallographic analysis shows heterodimeric GluN1-GluN2B ATDs that have a bi-lobed architecture composed of the regions previously called R1 and R2 in the structure of GluN1b-GluN2B ATD bound to an allosteric inhibitor, ifenprodil (Fig. 1)[24]. There are a number of differences between the structures of the apo-GluN1b-GluN2B ATD and the ifenprodil-GluN1b-GluN2B ATD[24]. The most apparent difference is the separation of GluN1b-R1 and GluN2B-R2 in the apo-GluN1b-GluN2B ATD due to the ~20° rigid-body opening of the GluN2B ATD bi-lobed structure in the apo-GluN1b-GluN2B ATD compared to that in ifenprodil-GluN1b-GluN2B ATD (Fig. 1d). This observation is consistent with previous work suggesting GluN2B ATD to have open-cleft and closed-cleft conformations in the absence and presence of ifenprodil, respectively, based on luminescence resonance energy transfer[29]. Another major difference is the rearrangement of the GluN1b and GluN2B subunits that involves a ~15° rotation relative to one another (Fig. 1e). This rearrangement brings the lower lobes (R2) of GluN1-GluN2B significantly closer together in the apo-GluN1b-GluN2B ATD compared with the ifenprodil-GluN1b-GluN2B ATD (Fig. 1e, Extended Data Fig. 2c). For example, the distance between Cαs of GluN1b Lys178 and GluN2B Asn184 in apo-GluN1b-GluN2B ATD is 4.4 Å closer than in the ifenprodil-GluN1b-GluN2B ATD (Fig. 1e).

Since the subunit arrangement in the apo-GluN1b-GluN2B ATD in our crystal structure is different from that previously observed in the ifenprodil-GluN1b-GluN2B ATD[22] we sought to validate its physiological relevance. Toward this end, we tested whether an inter-subunit disulfide bond can form at the subunit interface observed in the the apo-GluN1b-GluN2B ATD but not in the ifenprodil-GluN1b-GluN2B ATD in the context of the intact GluN1/GluN2B NMDA receptor by mutating GluN1 and GluN2B residues that are proximal to each other. We expected a spontaneous disulfide bond to form between the mutated cysteines in the intact GluN1/GluN2B NMDA receptor if the subunit interface observed in the crystal structure is physiological. We engineered cysteine residues at GluN1b Phe113/GluN2B Ala107 and GluN1b Gly331/GluN2B Glu75, expressed and purified the mutant GluN1b/GluN2B NMDA receptor in the context of the intact ion channel, and conducted Western blot analysis under non-reducing conditions to detect band shifts (Extended Data Fig. 3a). In the two selected positions, the disulfide bonds are formed only when the cysteine mutant (Extended Data Fig. 3) of GluN1 and that of GluN2B are co-expressed and detected by an anti-GluN1 and an anti-GluN2B Western blot in the absence of β-mercaptoethanol. When the cysteine mutants of one subunit is co-expressed with the wild type (WT) of the other subunit no disulfide bonds are formed, indicating that they are specifically formed by the engineered cysteines. Taken together, the above experiments show that the GluN1-GluN2B subunit arrangement observed in the apo-GluN1b-GluN2B ATD crystal structure exists in the context of the intact GluN1b/GluN2B NMDA receptor.

The apo-GluN1b-GluN2B ATD structure represents an active conformation of the ATD

To understand what functional state the crystal structure of the apo-GluN1b-GluN2B ATD may represent, we next attempted to stabilize the conformation observed in the crystal structure and assessed the ion channel activity. Toward this end, we engineered cysteines at the positions in the lower lobes (R2) of the GluN1b and GluN2B ATDs (GluN1b Ala175Cys/GluN2B Gln180Cys and GluN1b Lys178Cys/GluN2B Asn184Cys), which face each other and should "trap" the crystallized conformation by tethering the engineered cysteines with bi-functional methanthiosulfonate (bi-MTS) reagents (Fig. 2). The distances between the mutated residues are closer in apo-GluN1b-GluN2B ATD than in ifenprodil-GluN1b-GluN2B ATD as mentioned above (Fig. 1e). When bi-MTS shorter in length than M4M binds to the lower lobes of the GluN1b-GluN2B heterodimers, we reasoned that the conformation observed in the apo-GluN1b-GluN2B ATD with the open GluN2B bi-lobed architecture and the rearranged GluN1-GluN2B subunit orientation should be trapped. To test this prediction, we co-expressed the cysteine mutants of GluN1b and GluN2B in *Xenopus* oocytes and probed the effect of the bi-MTS reagents on the macroscopic current of NMDA receptor by two-electrode voltage clamp (TEVC). We initialized this experiment by testing bi-MTS with the four-carbon linker (M4M in Fig. 2a) since the estimated distances between the γ-sulfur atom of the mutated cysteines in the GluN1b Ala175Cys/GluN2B Gln180Cys and GluN1b Lys178Cys/GluN2B Asn184Cys mutants of apo-GluN1b-GluN2B ATD are ~10 Å and ~9 Å, respectively, roughly matching the length of M4M. The application of M4M to the GluN1b Ala175Cys/GluN2B Gln180Cys and GluN1b Lys178Cys/GluN2B Asn184Cys mutants potentiates the NMDA receptor currents by ~3–4-fold (Fig. 2b–c, Extended Data Fig. 4). No such effect is observed when the cysteine mutants of one subunit are co-expressed with the WT of the other subunit, indicating that the observed functional effect is specific to the engineered cysteines (Fig. 2a and Extended Data Fig. 5a–b). We suggest that this potentiating effect by the bi-MTS conformational trap favored the NMDA receptor ion channel to reside in the "active" form. The effect of M4M is observed both in the presence and absence of glycine and glutamate indicating that conformational alteration in the ATD is independent of agonist binding in the LBD. Furthermore, the potentiation effect was also observed when M2M was applied to both of the above mutant pairs, indicating that the GluN1b-GluN2B distance in R2 may move even closer than observed in the crystal structure, consistent with the single-particle electron cryomicroscopy (cryo-EM) structures shown in the next section of this article. By contrast, when adding M8M, a bi-MTS agent that is 4–5 Å longer than the inter-cysteine distances observed in the apo-GluN1b-GluN2B ATD, no potentiating effect was observed, supporting the view that the distance between the R2 lobes of GluN1b-GluN2B must be reduced during activation (Fig. 2c, Extended Data Fig. 5). Finally, when M4M was applied in the presence of ifenprodil, we observe little or no potentiating effect indicating that it traps the active conformation of GluN1b-GluN2B ATDs but not the inhibited conformation as represented by the crystal structure of the ifenprodil-GluN1b-GluN2B ATD (Fig. 2b, d). Taken together, these experiments indicate that the protein conformation observed in the crystal structure of the apo-GluN1b-GluN2B ATD likely represents the active conformation that facilitates ion channel opening.

Cryo-EM structures of intact GluN1b-GluN2B NMDA receptors

How do the changes in the GluN1-GluN2B ATD conformation alter subunit arrangement and inter-ATD-LBD interactions to ultimately mediate gating of the ion channel? To answer this question, we obtained cryo-EM structures of the intact heterotetrameric rat GluN1b-GluN2B NMDA receptor ion channel in the presence of glycine and L-glutamate and in the absence of ifenprodil. The cryo-EM structures were reconstructed at resolutions better than 7 Å and revealed clear secondary structure elements (Fig. 3, Extended Data Fig. 6–7 and Extended Data Table 2). The cryo-EM structures show conservation of general features observed in the recent full length NMDA receptor crystal structures, including a dimer of GluN1-GluN2B heterodimers arrangement at the ATD and LBD layers, the domain swap between the ATD and LBD, and pseudo-four-fold symmetrical subunit arrangement at the TMD[22,23]. Importantly, 3D classification of the cryo-EM data revealed different conformational states present in the dataset (Fig. 3). Overall, there are roughly three distinct conformations, which we define as ‘non-active1,’ ‘non-active2,’ and ‘active’ (Fig. 3). When compared to the crystal structure of the intact NMDA receptors bound to ifenprodil, glycine, and L-glutamate[22,23], which represent the allosterically inhibited functional state, all of the 3D classes contain a GluN2B ATD open bilobed architecture, with a ~14–21° opening similar to the crystal structure of the apo-GluN1b-GluN2B ATD. This opening of the GluN2B ATD increases the distance between the two GluN1 ATDs by as much as ~29 Å in the intact NMDA receptor compared to the ifenprodil-bound form (Fig. 3). The comparison shows that, upon ifenprodil binding, the R1 lobe moves relative to the LBD and TMD to close the bi-lobed architecture of the GluN2B ATD, as well as the gap between the two GluN1 ATDs to inhibit receptor activity.

The two 3D classes, ‘non-active 1’ and ‘non-active 2,’ are both in the state where agonists are bound to the LBD but the ion channel is closed. When focusing on the ATD, both ‘non-active 1’ and ‘non-active 2’ do not display the ~15° rotation of the GluN1b and GluN2B subunits relative to one another as observed in the crystal structure of the apo-GluN1b-GluN2B ATD, which represents a conformation that can activate the receptor. The arrangements of the dimer of the GluN1b-GluN2B ATD dimers (Fig. 4c), as well as the dimer of GluN1b-GluN2B LBD dimers (Fig. 5a,c,e) remain similar to those observed in the crystal structure of the intact NMDA receptor (‘inhibited’ conformation) (Fig. 4 and 5). Consequently, the ion channel pores at the TMD remain closed, confirming that both cryo-EM classes likely represent non-gating or ‘non-active’ conformations. The difference in ‘non-active 1’ and ‘non-active 2’ is the extent of bi-lobe opening in the GluN2B ATD where ‘non-active 2’ has a ~7° more open conformation resulting in ~13 Å larger separation between the GluN1 ATDs (Fig. 3). Even though we tentatively call these two conformations ‘non-active,’ it remains uncertain whether they represent functional states equivalent to the ‘pre-open’ state observed in non-NMDA receptors[17,30] or a ‘desensitized’ state.

Active conformation

One of the cryo-EM classes, ‘active’ (Fig. 3), shows the cleft of the bilobed GluN2B ATD architecture opened by ~22° and a GluN1b-GluN2B heterodimeric subunit rotated by ~12°, compared to the ifenprodil-bound intact NMDA receptors, which is strikingly similar to the

apo-GluN1b-GluN2B ATD crystal structure representing the ‘active’ ATD conformation (Fig. 1 and 4e and Extended Data Fig. 7). In the heterotetrameric NMDA receptor, the GluN1b-GluN2B heterodimer pairs rotate by ~12° in opposite directions (Fig. 4f). Importantly, this 3D structure of the ‘active’ conformation of the ATD also shows large differences in the subunit arrangement of LBDs compared to the other 3D classes representing ‘non-active’ ATDs, and is also different from the recent crystal structures of the glycine, L-glutamate, and ifenprodil complexes[22,23]. Specifically, when transitioning from the ‘non-active 2’ to ‘active’ conformation, the two pairs of GluN1b-GluN2B LBD heterodimers rotate by ~13.5° (Fig. 5b,d,f). These subunit movements in the LBD cause movement of the residues at the LBD-TMD linkers (Fig. 5). For example, when focusing on the residues located right above the pore formed by the M3 TMD helices, the consorted movement between the ATD and LBD going from “non-active 2” to “active” described above causes a vertical movement of GluN1b Arg684 and the lateral separation of GluN2B Glu658 by 7 Å and 11 Å, respectively, to dilate the gating ring, a movement that is likely to lead to ion channel gating[31] (Fig. 5d,f, Fig. 6, Supplementary Video 1–2). Thus, this cryo-EM class is structurally and functionally consistent with an ‘active’ conformation for GluN1/GluN2B NMDA receptors. While there is clear density for most of the domains in the ‘active’ conformation of the receptor, the density for the TMD is not resolved in sufficient detail to directly observe opening of the ion channel, as is the case for the AMPA receptors[17]. This may indicate that the TMD domain is structurally more variable in activated receptors compared to non-active receptors. Finally, the comparison of the cryo-EM classes with GluA2 AMPA receptor in the ‘pre-open’ state, which represents a closed channel[17,30], shows that there is a greater difference between the ‘active’ and ‘pre-open’ states than between the ‘non-active 2’ and ‘pre-open’ states (Extended Data Fig. 8), consistent with our observation that the TMD ion channel in the ‘non-active’ structures are also closed.

Conclusion

We report conformational changes in multiple domains that are experimentally linked to activation of mammalian GluN1b/GluN2B NMDA receptors. The activation requires opening of the bi-lobed architecture of the GluN2B ATD and reorientation of the heterodimeric arrangement in the GluN1b-GluN2B ATD as captured at high-resolution by the crystal structure presented here. These changes lead to rotated GluN1b-GluN2B heterodimeric pairs in both the ATD and LBD, causing dilation of the gating ring. The mechanistic understanding gained in the current study represents an important first step in understanding the sophisticated activation schemes[26,32,33] that are essential for mammalian NMDA receptor function.

Methods

No statistical methods were employed to predetermine sample size.

Production of GluN1b/GluN2B ATD, GluN1b/GluN2B NMDA receptors, and Fab fragment

The constructs of GluN1b and GluN2B ATDs are identical to those used in our previous study and were expressed and purified in the same way[24]. The purified protein was

deglycosylated by endoglycosidase F1. Monoclonal antibodies (mouse immunoglobulin-γ (IgG)) that bind rat GluN2B ATD were obtained by immunizing mice with the purified intact GluN1-GluN2B NMDA receptors using the standard protocol. IgGs were purified from hybridoma cell culture supernatant by Protein-A Sepharose (GE healthcare). Fab fragments of the antibody were obtained by papain proteolysis followed by re-chromatographing onto Protein-A Sepharose to remove Fc. The purified GluN1b-GluN2B ATD and Fab were mixed, and the ATD-Fab complex was isolated by Superdex200 (10/300; GE Healthcare). The intact tetrameric GluN1b/GluN2B NMDA receptors were expressed and purified as previously described[22].

Crystallization, Data Collection, and Structural determination of apo-GluN1b-GluN2B ATD

The purified GluN1b-GluN2B ATD-Fab complex was concentrated to 8 mg/ml and dialyzed against a buffer containing 10 mM Tris-HCl (pH 8.0) and 50 mM NaCl. The crystals were grown at 18°C by the hanging-drop vapor diffusion method. GluN1b-GluN2B ATD-Fab complex was mixed with a half volume of reservoir solution (3–5 μl total drop size), which contained 0.1 M sodium acetate (pH 4.5), 27% PEG3350, 2.2 M sodium formate, and 0.05 M calcium chloride. Cryoprotection was achieved by supplying 8% glycerol to the crystallization condition. Crystals were flash-frozen in liquid nitrogen. Datasets were collected at the wavelength of 1.0 Å and at the 23ID-D beamline in the Advanced Photon System in the Argonne National Laboratory and processed using HKL2000 [34] (Extended Data Table 1). The crystal structure of GluN1b-GluN2B ATD-Fab17 complex was solved by molecular replacement using the coordinate of GluN1b/GluN2B ATD (PDB code: 3QEL) and Fab (PDB code: 1BAF) and by using the program Phaser[35]. The model refinement was done using the program Phenix[36].

Electrophysiology

GluN1-4b/GluN2B NMDA receptors were expressed by injecting cRNAs at a 1:2 ratio (GluN1: GluN2, w/w) into defolliculated *Xenopus laevis* oocytes (0.05–0.15 ng total per oocyte). After 24–48 hours incubation at 18°C, currents were measured by two-electrode voltage clamp in a solution containing 5 mM HEPES, 100 mM NaCl, 0.3 mM $BaCl_2$ and 10 mM Tricine at pH 6.5 (adjusted with KOH) using agarose-tipped microelectrode (0.4–1.0 MΩ) at the holding potential of −60 mV. Currents were evoked by application of 100 μM glycine and L-glutamate. For MTS experiments, fresh stock of MTS reagents were made and added to the recording buffers at the final concentration of 200 μM. The data were analyzed using the program Pulse (HEKA) and the graphs were generated by the program Kaleidagraph (Synergy).

Cysteine crosslinking and Western blot

Recombinant WT and mutant GluN1-4b/GluN2B NMDA receptors (GluN2B CTD truncated as in Extended Data Fig. 1), were expressed in the *Spodoptera frugiperda (Sf9)* baculovirus system as described previously[22]. The infected cell pellets were solubilized in a buffer containing 50 mM HEPES pH 7.3, 200 mM NaCl, 0.5 % LMN, and 1 mM PMSF. The GluN1-4b/GluN2B NMDA receptor proteins were purified by Strep-Tactin Sepharose (IBA) and subjected to 7% SDS-polyacrylamide gel electrophoresis in the presence and absence of 100 mM β-mercaptoethanol. The proteins were transferred to nitrocellulose

membranes (GE healthcare). The membranes were blocked with 5% milk in a phosphate saline buffer containing 0.05% Tween-20, incubated with mouse monoclonal anti-GluN1 antibody (MAB1586, Millipore) or anti-GluN2B antibody (AB93610, Abcam), followed by HRP-conjugated anti-mouse secondary antibodies (GE healthcare). The ECL detection kit (GE healthcare) was used to visualize bands.

Cryo-EM specimen preparation and image acquisition

Purified GluN1b/GluN2B NMDA receptor at 2 mg/ml was placed on C-flat™ 1.2/1.3 Cu 400 mesh grids (Protochips), which had previously been subjected to glow discharge for 45 s at 15 mA, and plunge-frozen using an FEI Vitrobot Mark 2 with a 3 s blot time and at relative humidity between 85% and 95%. The data were collected on an FEI Titan Krios microscope operating at 300 kV. Movies were collected on a Gatan K2 Summit direct electron detector (Gatan, Inc.) in super resolution mode with a pixel size of 0.655 Å per super resolution pixel. Each exposure was 21 s long and recorded as a movie of 70 frames. The exposure per frame as reported by Digital Micrograph (Gatan, Inc.) was ~1.4 $e^-/Å^2$, which corresponds to an exposure of ~8 electrons/pixel/s on the camera. Movies were collected at a range of underfocus between ~1.0 μm and ~2.5 μm.

Image processing

Super-resolution movie frames were initially corrected for magnification distortion[37]. The frames were then downsampled by a factor of 2 using Fourier cropping to a pixel size of 1.31 Å, motion-corrected and exposure filtered using Unblur[38] and the microscope CTF was determined using CTFFIND4[39] on motion-corrected but non-exposure filtered movie sums. ~90k particles were picked automatically then verified manually from the aligned movie sums which had been exposure filtered, but not noise restored resulting in a strong low pass filter. The picked particles were extracted into 256×256 boxes. Initial particle alignment parameters were assigned by a brute force search in Frealign v9[40], sampling every 5° and limiting the resolution to 15 Å using a previously determined structure as a reference. These parameters were further refined and classified into six 3D classes with Frealign. For classes 1, 3 and 6 the highest resolution included in the alignment was 8 Å, for class 4 the highest included resolution was 12 Å and for class 5 it was 6.5 Å. The resulting resolutions as determined by the 0.143 cut-off[41] were 5.0 – 6.7 Å (Extended Data Fig. 6). Maps were rendered using UCSF Chimera[42], after applying a bfactor of −600 $Å^2$.

Model building

The GluN1a/GluN2B crystal structure (PDB ID: 4PE5[22]) was docked into the cryo-EM maps followed by rigid-body fitting of the individual ATD R1 and R2 lobes and LBDs of both GluN1 and GluN2B into the cryo-EM maps using COOT[43]. Both the rat GluN1a/GluN2B crystal structure (PDB ID: 4PE5[22]) and *Xenopus* GluN1/GluN2B NMDA receptor (PDB ID: 4TLM[23]) were used to model the TMD. The resulting models were manually modified to fit into the density using COOT[43] and refined against the cryo-EM maps using Phenix real space refinement[44]. Refinement statistics are shown in Extended Data Table 2. Class X and Class Y are similar to ‘Non-Active 2.’

Extended Data

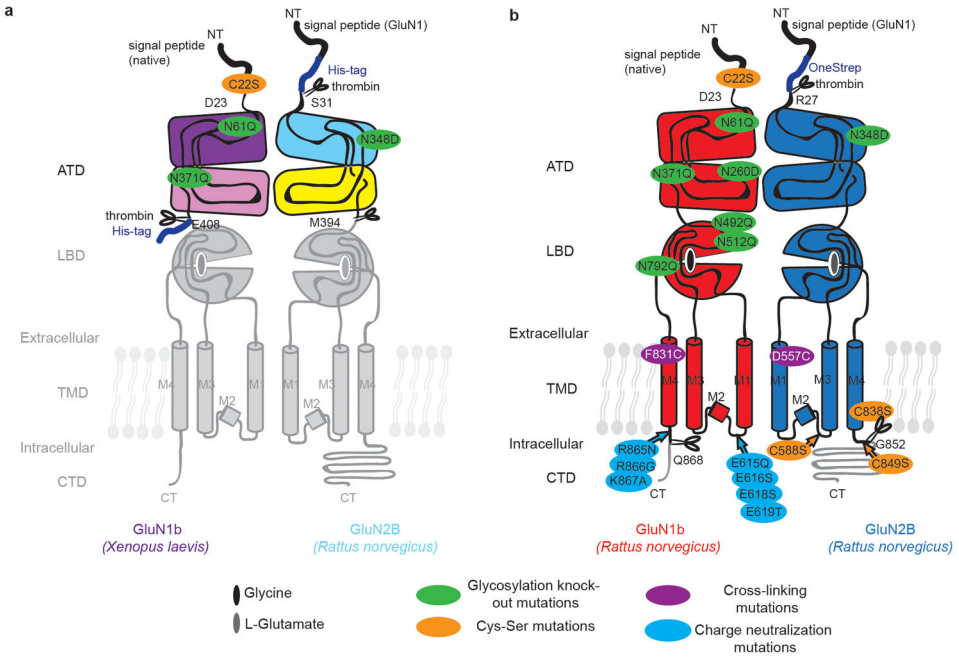

Extended Data Figure 1. Domain organization and constructs

a, The construct design for GluN1b and GluN2B ATD used in this study. GluN1b from *Xenopus laevis* is combined with GluN2B from rat as in the previous study on the ATD (Karakas et al, 2011). **b,** The construct design for the intact GluN1b/GluN2B NMDA receptors from rat. A similar construct was used in previous studies shown to be fully functional (Karakas and Furukawa, 2014).

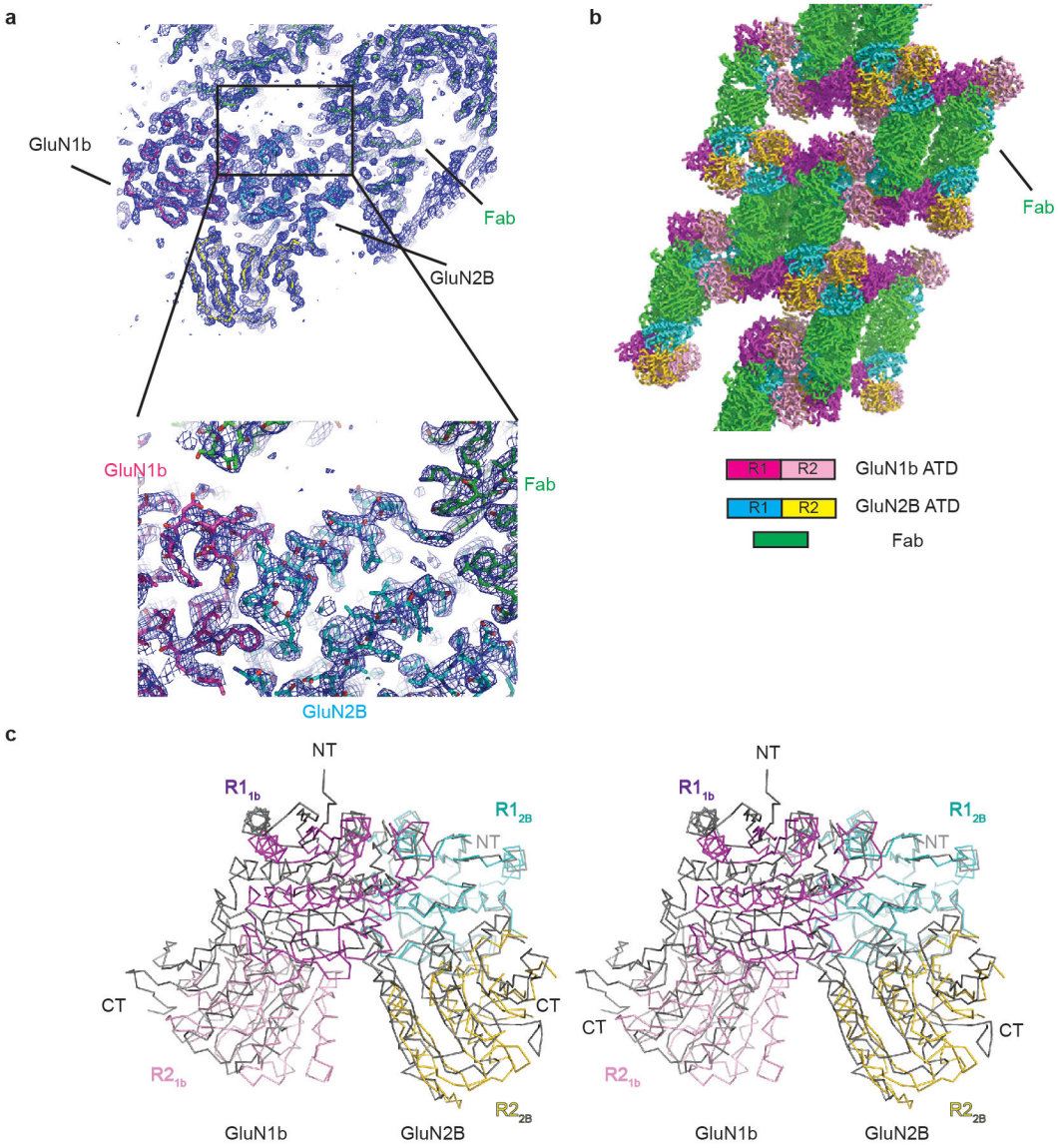

Extended Data Figure 2. Structure of the apo-GluN1b-GluN2B ATD

a, Representative 2Fo-Fc electron density map contoured at 1.2 σ showing continuous density throughout GluN1b, GluN2B, and Fab. The quality of the electron density map is at a sufficient level to model amino acid side chains (see lower panel). **b,** Crystal packing of GluN1b-GluN2B ATD-Fab showing that the packing is mediated robustly by Fab molecules (green). The color code for the ATD is the same as in Fig. 1. **c,** Comparison of the apo-GluN1b-GluN2B ATD and ifenprodil-GluN1b-GluN2B ATD (grey) by stereo presentation. Color coding for the apo-GluN1b-GluN2B ATD is the same as in Fig. 1. Here the two structures are superimposed at GluN2B R1.

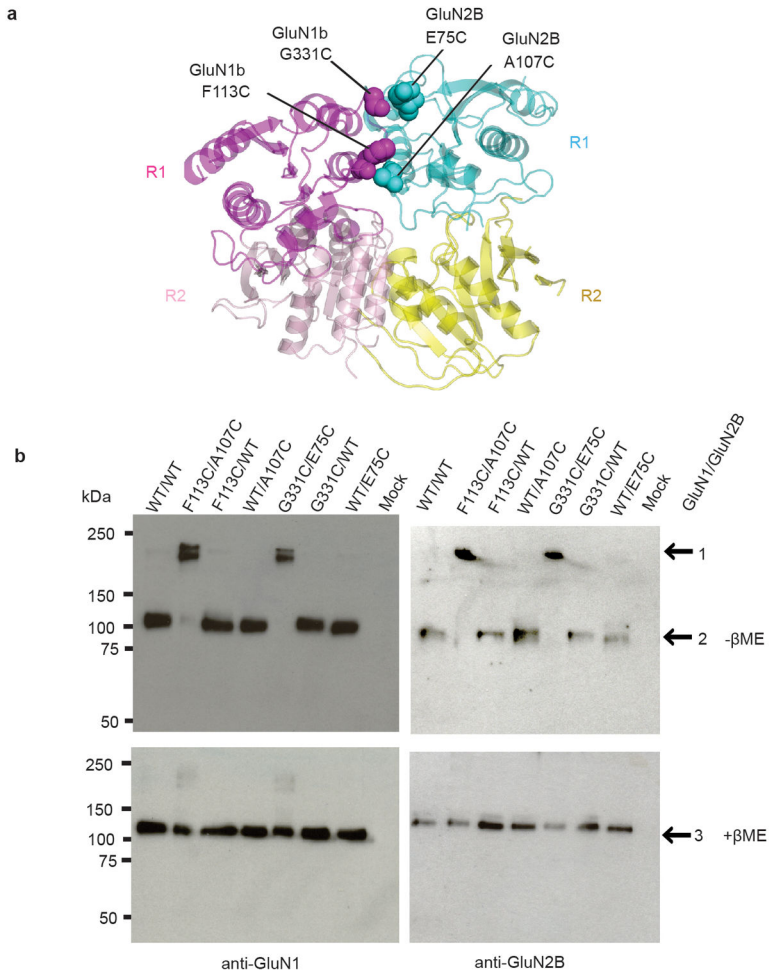

Extended Data Figure 3. Validation of the crystal structure by disulfide cross-linking

a, Crystal structure of the apo-GluN1b-GluN2B ATD showing locations of the mutated residues, GluN1b Phe113, GluN1b Gly331, GluN2B Ala107, and GluN2B Glu75 in spheres. **b,** Western blots using anti-GluN1 (left) and anti-GluN2B (right) antibodies on purified intact GluN1b/GluN2B NMDA receptor that lacks the CTD. Upper and lower panels are blots run in the absence and presence of β-mercaptoethanol (βME), respectively. Bands highlighted by Arrow 1 are consistent with the molecular weight of GluN1-GluN2B heterodimers whereas those highlighted by Arrow 2 and 3 are consistent with the molecular weights of monomers of GluN1-4b and GluN2B.

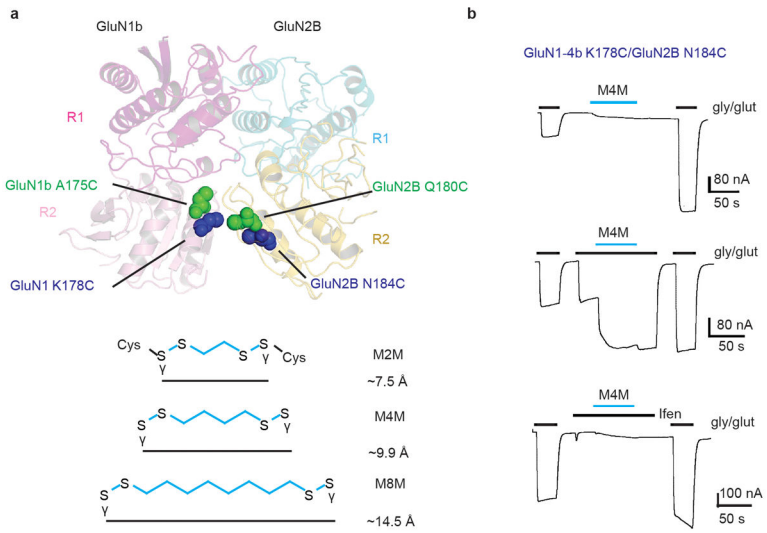

Extended Data Figure 4. Conformational trap shows the apo-GluN1b-GluN2B ATD structure to represent 'active' form-II

a, Location of engineered cysteines in the crystal structure of the apo-GluN1b-GluN2B ATD. The cysteine mutant pairs, GluN1-4b Ala175Cys/GluN2B Gln180Cys (in green spheres) and GluN1-4b Lys178Cys/GluN2B Asn184Cys (in blue spheres) are co-expressed in *Xenopus* oocytes and cross-linked by bifunctional MTS with different linker lengths (M2M, M4M, and M8M). **b,** Application of 200 μM M4M in the presence or absence of 100 μM agonists (glycine (gly)/glutamate (glut)) potentiates the macroscopic current measured at the holding potential of −60 mV by TEVC. No potentiation was observed when M4M was applied in the presence of ifenprodil (Ifen). Shown here are the representative recording profiles for the GluN1-4b Lys178Cys/GluN2B Asn184Cys pair.

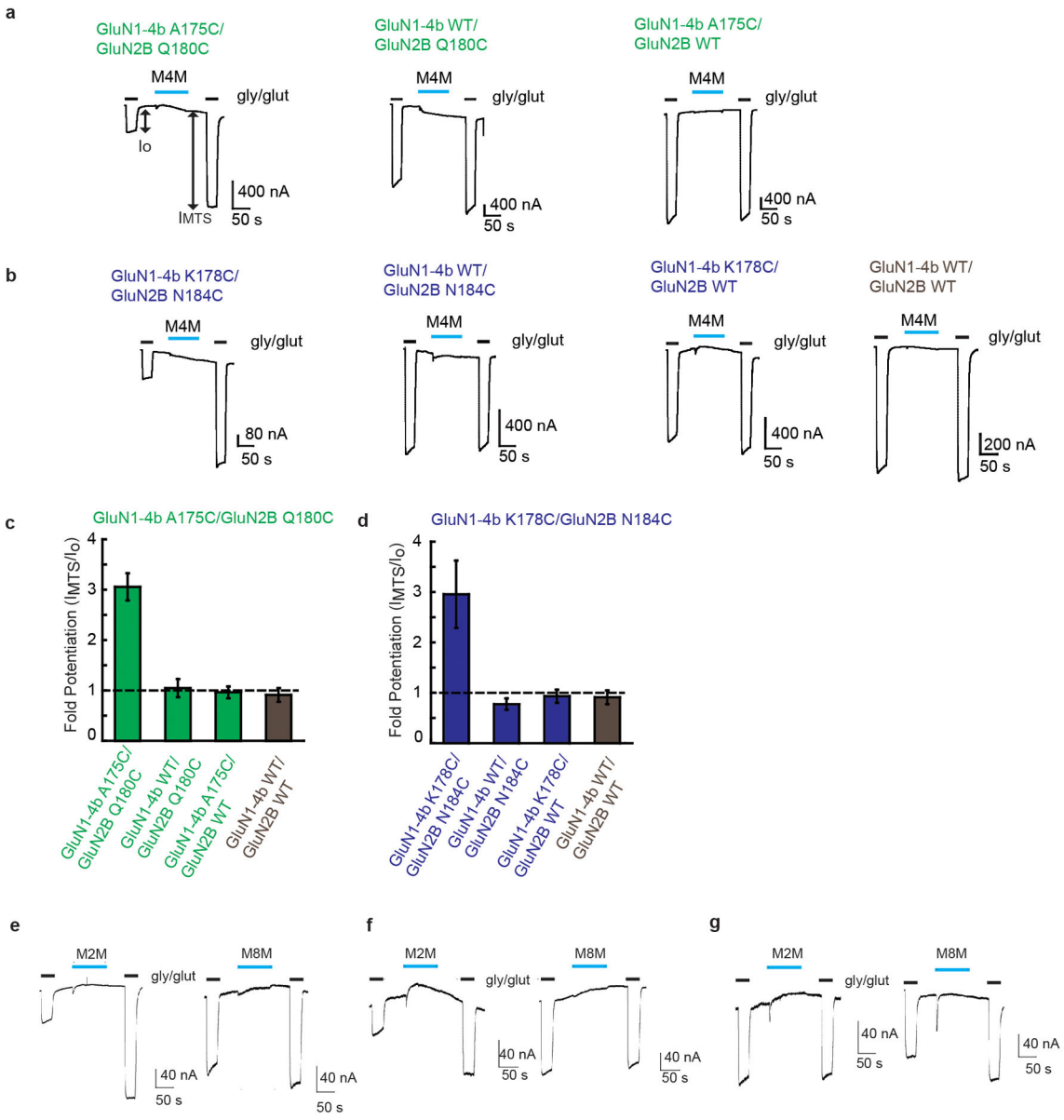

Extended Data Figure 5. Effect of bi-MTAs on cysteine mutants

a–b, M4M specifically traps the active conformation at the engineered cysteines. Representative electrophysiological traces for the mutant pairs, GluN1-4b Ala175Cys/ GluN2B Gln180Cys (in green spheres) and GluN1-4b Lys178Cys/GluN2B Asn184Cys as well as mutant and WT pairs. The experiments are conducted by TEVC as in Fig. 2. The potentiation by M4M (represented by I_{MTS}/I_o) is only observed when both GluN1 and GluN2B cysteine mutants are co-expressed. No potentiation was observed when the cysteine mutant of one subunit is combined with the WT of the other, indicating that the effect of M4M modification is specific and validating the relevance of the experiments. **c,d,** Bar graphs presenting the degree of potentiation from the recordings in panel (a) and (b). Error bars represent ±S.D. for data obtained from five different oocytes ($n = 5$) per mutant combination. **e–g,** M2M but not M8M potentiates the mutant GluN1b/GluN2B NMDA

receptor. The same experiment as above or in Fig. 2 was conducted using M2M or M8M on GluN1-4b Ala175Cys/GluN2B Gln180Cys **(e)** GluN1-4b Lys178Cys/GluN2B Asn184Cys **(f)**, and GluN1-4b WT/GluN2B WT **(g)**. Shown are representative electrophysiological recordings used to estimate the degree of bi-MTS potentiation presented in Fig. 2c.

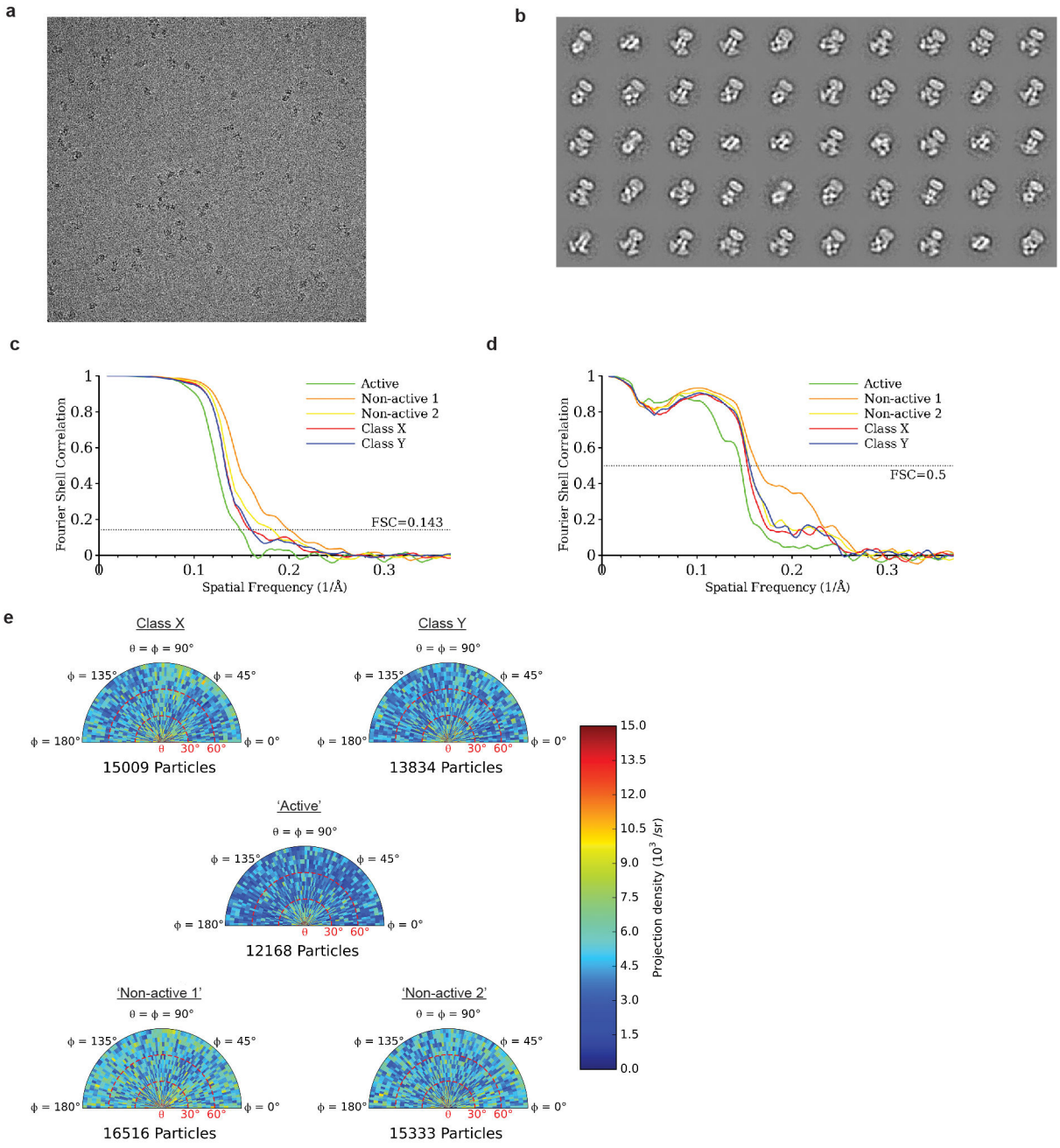

Extended Data Figure 6. Cryo-EM analysis on GluN1b/GluN2B NMDA receptors

a, Representative motion-corrected image collected at 22.5K magnification. **b,** 2D class averages. **c–d,** FSC curves for unmasked data **(c)** and model vs. EM map **(d)**. Class X and Y are similar to 'Non-active 2.' **e,** Orientation plots for each class, plotting the distribution of

Euler angles assigned to all particles contributing to that class with an occupancy of at least 80%. For each class, the number of particles which have that class as their highest occupancy value is also shown.

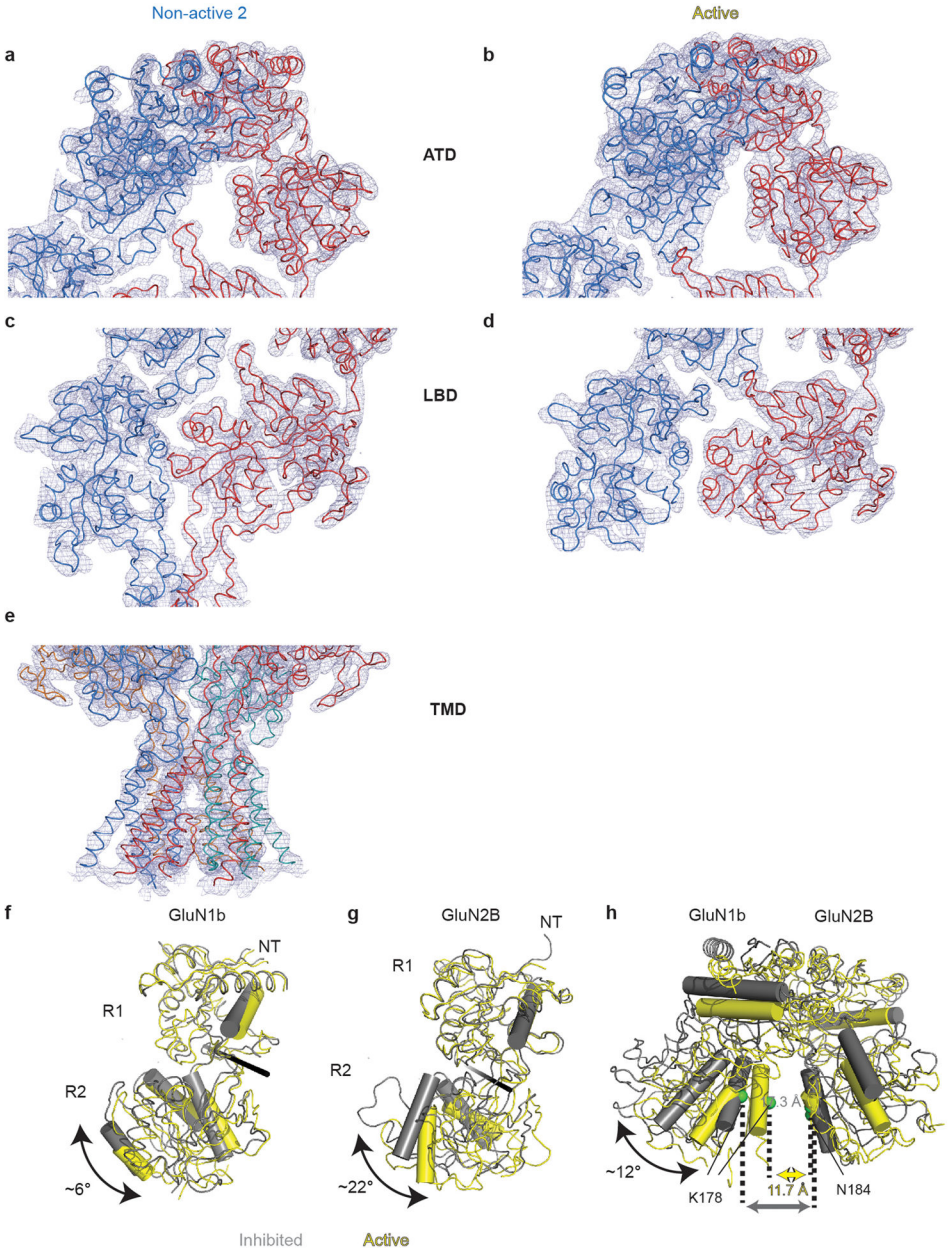

Extended Data Figure 7. Representative cryo-EM density, model fit, and structural comparison of the ATD in inhibited and active conformations of cryo-EM structures

Here, the cryo-EM maps for ‘non-active 2’ and ‘active’ 3D classes are shown along with the refined models. Densities are shown at the ATD and LBD **(a–d)** for both of the 3D classes and at the TMD **(e)** for ‘non-active 2.’ **f–g,** Superposition of R1 lobes of GluN1b **(f)** and GluN2B **(g)** illustrates the relative ‘opening’ between R1 and R2 lobes in the ‘inhibited’ and ‘active’ forms of intact NMDA receptors. The extent of GluN2B ATD opening is similar to

that observed between the crystal structures of the ifen-GluN1b-GluN2B ATD and the apo-GluN1b-GluN2B ATD as in Fig. 1. GluN1b and GluN2B ATDs are shown in gray and yellow for the ‘inhibited’ and ‘active’ states, respectively. **h,** Comparison of the GluN1b-GluN2B ATD heterodimers between ifenprodil ‘inhibited’ and ‘active’ cryo-EM structures. Superposition of the GluN2B R1 lobes reveals a ~12° rotation of the GluN1b ATD relative to the GluN2B ATD in the similar manner to the crystal structure of the apo-GluN1b-GluN2B ATD as in Fig. 1. The black rods indicate the axis of rotation between the two cryo-EM structures. The distance of the R2 lobes in the GluN1b-GluN2B heterodimers is measured between Cαs of GluN1b Lys178 and GluN2B Asn184 (green spheres).

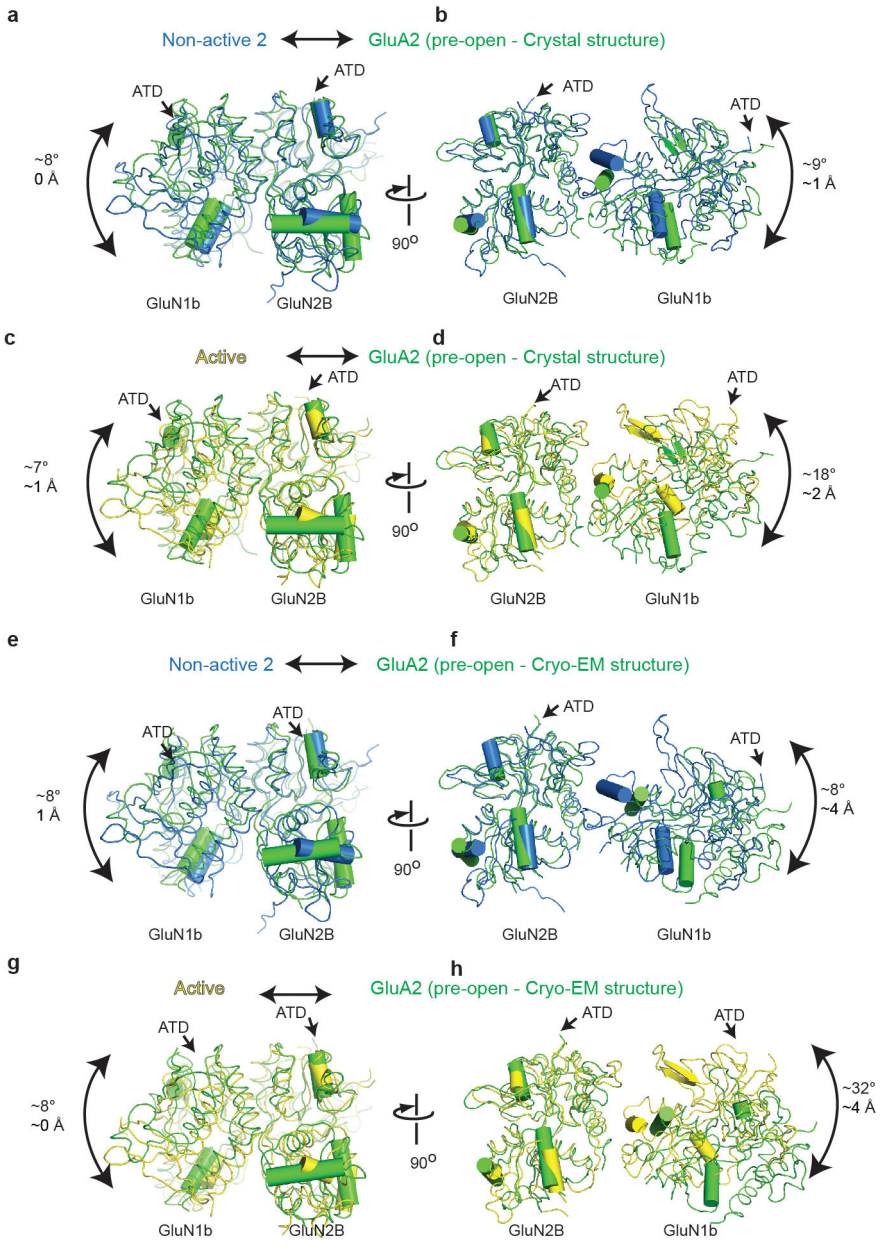

Extended Data Figure 8. Structural comparison of the GluN1-GluN2B LBD in 'non-active' and 'active' conformations to the GluA2 LBD in 'pre-open' state

a–d, The crystal structure of GluA2 AMPA receptor in the 'pre-open' state (PDB ID: 4U1W, shown in green) aligned with the structures of GluN1-GluN2B in the 'non-active 2' (blue) **(a,b)** and 'active' conformation (yellow) **(c,d)** by superposing the LBDs of GluN2B onto GluA2. **e–h,** The equivalent superposition with the cryo-EM structure of GluA2 AMPA receptor in the 'pre-open' state (PDB: 4UQ6, shown in green). The overlaid structures are viewed through the LBD heterodimer interface **(a,c or e,g)** and the dimer of heterodimer interface **(b,d or f,h)**. Here, the GluN2B LBD of the GluN1b-GluN2B NMDA receptor is superposed onto the LBD of the GluA2 AMPA receptor and the shift of the GluN1 LBD is measured with respect to the other GluA2 LBD. The homodimeric arrangement of GluA2 AMPA receptor in the 'pre-open' state is similar to the heterodimeric arrangements of GluN1b-GluN2B NMDA receptors in both 'non-active 2' and 'active' states **(a,c or e,g)**. However, when the dimer of homodimer arrangement of GluA2 AMPA receptor is compared to the dimer of heterodimers arrangement of the GluN1b-GluN2B NMDA receptor, a greater difference is observed for the 'active' NMDA receptor **(d,h)** than the 'non-active 2' NMDA receptor **(b,f)**. Here, the 'non-active 2' NMDA receptor as in Fig. 3 is subjected to superposition. The 'non-active 1' and 'non-active 2' NMDA receptors have similar subunit arrangements in the LBD. The numbers in each panel represent degrees of rotations and translations.

Extended Data Table 1

Data collection and refinement statistics for x-ray crystallography

	Apo-GluN1b/GluN2B ATD–Fab17
Data collection	
Space group	C2
Cell dimensions	
a, *b*, *c* (Å)	247.4, 80.0, 181.4
α, *β*, *γ*(°)	90.0, 127.2, 90.0
Resolution (Å)	50-2.90(2.93–2.90) *
R_{merge}	0.099 (0.602)
$I/\sigma I$	8.5 (1.84)
Completeness (%)	91.4 (93.0)
Redundancy	4.0 (3.5)
Refinement	
Resolution (Å)	30-2.9
No. reflections	57,592
R_{work}/R_{free}	0.257/0.296
No. atoms	
Protein	15,896
Ion (Na)	1
Water	112
B-factors	
Protein	52.6

	Apo-GluN1b/GluN2B ATD–Fab17
Ligand/ion	47.6
Water	38.5
R.m.s deviations	
Bond lengths (Å)	0.010
Bond angles (°)	1.276

* Highest resolution shell is shown in parenthesis.

Extended Data Table 2

Refinement statistics for the cryo-EM structures

	Active	Non-Active 1	Non-Active 2	Class X	Class Y
PDB ID	5FXG	5FXH	5FXI	5FXJ	5FXK
EMDB ID	EMD-3352	EMD-3353	EMD-3354	EMD-3355	EMD-3356
Refinement					
Resolution (Å)	6.8	6.1	6.4	6.5	6.4
Map to Model CC	0.77	0.79	0.80	0.78	0.80
No. atoms					
Protein	12,693	15,578	15,381	15,475	15,598
R.m.s deviations					
Bond lengths (Å)	0.003	0.006	0.003	0.004	0.005
Bond angles (°)	0.55	0.55	0.60	0.58	0.55
Ramachandran					
Favored (%)	88.3	90.4	90.2	88.0	88.8
Allowed (%)	11.5	9.2	9.4	11.4	10.7
Disallowed (%)	0.2	0.5	0.4	0.6	0.5

Supplementary Material

Refer to Web version on PubMed Central for supplementary material.

Acknowledgments

We thank staff at the 23-ID beamlines at the Advanced Photon System in the Argonne National Laboratory. We are grateful to Zhiheng Yu, Chuan Hong, and Rick Huang at the Janelia Research Center (JRC)/HHMI EM facility for their excellent support. This work was supported by the National Institutes of Health (MH085926 and GM105730 to HF), the Stanley Institute of Cognitive Genomics (to HF), Japan Society for the Promotion of Science (to NT), Burroughs Wellcome Fund Collaborative Research Travel Grant (to HF), the Robertson Research Fund of Cold Spring Harbor Laboratory (to HF), and the Visiting Scientist program of the JRC to allow HF to conduct cryo-EM work.

References

1. Traynelis SF, et al. Glutamate receptor ion channels: structure, regulation, and function. Pharmacol Rev. 2010; 62:405–496. DOI: 10.1124/pr.109.002451 [PubMed: 20716669]
2. Benveniste M, Mayer ML. Structure-activity analysis of binding kinetics for NMDA receptor competitive antagonists: the influence of conformational restriction. British journal of pharmacology. 1991; 104:207–221. [PubMed: 1686203]

3. Clements JD, Westbrook GL. Activation kinetics reveal the number of glutamate and glycine binding sites on the N-methyl-D-aspartate receptor. Neuron. 1991; 7:605–613. [PubMed: 1681832]
4. Johnson JW, Ascher P. Glycine potentiates the NMDA response in cultured mouse brain neurons. Nature. 1987; 325:529–531. DOI: 10.1038/325529a0 [PubMed: 2433595]
5. Nowak L, Bregestovski P, Ascher P, Herbet A, Prochiantz A. Magnesium gates glutamate-activated channels in mouse central neurones. Nature. 1984; 307:462–465. [PubMed: 6320006]
6. Mayer ML, Westbrook GL, Guthrie PB. Voltage-dependent block by Mg2+ of NMDA responses in spinal cord neurones. Nature. 1984; 309:261–263. [PubMed: 6325946]
7. Mayer ML, MacDermott AB, Westbrook GL, Smith SJ, Barker JL. Agonist- and voltage-gated calcium entry in cultured mouse spinal cord neurons under voltage clamp measured using arsenazo III. J Neurosci. 1987; 7:3230–3244. [PubMed: 2444678]
8. Granger AJ, Nicoll RA. Expression mechanisms underlying long-term potentiation: a postsynaptic view, 10 years on. Philos Trans R Soc Lond B Biol Sci. 2014; 369:20130136. [PubMed: 24298139]
9. Paoletti P, Bellone C, Zhou Q. NMDA receptor subunit diversity: impact on receptor properties, synaptic plasticity and disease. Nat Rev Neurosci. 2013; 14:383–400. DOI: 10.1038/nrn3504 [PubMed: 23686171]
10. Armstrong N, Sun Y, Chen GQ, Gouaux E. Structure of a glutamate-receptor ligand-binding core in complex with kainate. Nature. 1998; 395:913–917. DOI: 10.1038/27692 [PubMed: 9804426]
11. Furukawa H, Singh SK, Mancusso R, Gouaux E. Subunit arrangement and function in NMDA receptors. Nature. 2005; 438:185–192. [PubMed: 16281028]
12. Mayer ML. Crystal structures of the GluR5 and GluR6 ligand binding cores: molecular mechanisms underlying kainate receptor selectivity. Neuron. 2005; 45:539–552. DOI: 10.1016/j.neuron.2005.01.031 [PubMed: 15721240]
13. Hansen KB, Furukawa H, Traynelis SF. Control of assembly and function of glutamate receptors by the amino-terminal domain. Mol Pharmacol. 2010; 78:535–549. DOI: 10.1124/mol.110.067157 [PubMed: 20660085]
14. Gielen M, Siegler Retchless B, Mony L, Johnson JW, Paoletti P. Mechanism of differential control of NMDA receptor activity by NR2 subunits. Nature. 2009; 459:703–707. [PubMed: 19404260]
15. Yuan H, Hansen KB, Vance KM, Ogden KK, Traynelis SF. Control of NMDA receptor function by the NR2 subunit amino-terminal domain. The Journal of neuroscience. 2009; 29:12045–12058. DOI: 10.1523/JNEUROSCI.1365-09.2009 [PubMed: 19793963]
16. Zhu S, Paoletti P. Allosteric modulators of NMDA receptors: multiple sites and mechanisms. Curr Opin Pharmacol. 2015; 20:14–23. DOI: 10.1016/j.coph.2014.10.009 [PubMed: 25462287]
17. Meyerson JR, et al. Structural mechanism of glutamate receptor activation and desensitization. Nature. 2014; 514:328–334. DOI: 10.1038/nature13603 [PubMed: 25119039]
18. Karakas E, Regan MC, Furukawa H. Emerging structural insights into the function of ionotropic glutamate receptors. Trends Biochem Sci. 2015; 40:328–337. DOI: 10.1016/j.tibs.2015.04.002 [PubMed: 25941168]
19. Regan MC, Romero-Hernandez A, Furukawa H. A structural biology perspective on NMDA receptor pharmacology and function. Curr Opin Struct Biol. 2015; 33:68–75. DOI: 10.1016/j.sbi.2015.07.012 [PubMed: 26282925]
20. Sobolevsky AI, Rosconi MP, Gouaux E. X-ray structure, symmetry and mechanism of an AMPA-subtype glutamate receptor. Nature. 2009; 462:745–756. [PubMed: 19946266]
21. Kumar J, Schuck P, Mayer ML. Structure and assembly mechanism for heteromeric kainate receptors. Neuron. 2011; 71:319–331. DOI: 10.1016/j.neuron.2011.05.038 [PubMed: 21791290]
22. Karakas E, Furukawa H. Crystal structure of a heterotetrameric NMDA receptor ion channel. Science. 2014; 344:992–997. DOI: 10.1126/science.1251915 [PubMed: 24876489]
23. Lee CH, et al. NMDA receptor structures reveal subunit arrangement and pore architecture. Nature. 2014; 511:191–197. DOI: 10.1038/nature13548 [PubMed: 25008524]
24. Karakas E, Simorowski N, Furukawa H. Subunit arrangement and phenylethanolamine binding in GluN1/GluN2B NMDA receptors. Nature. 2011; 475:249–253. DOI: 10.1038/nature10180 [PubMed: 21677647]

25. Karakas E, Simorowski N, Furukawa H. Structure of the zinc-bound amino-terminal domain of the NMDA receptor NR2B subunit. Embo J. 2009; 28:3910–3920. DOI: 10.1038/emboj.2009.338 [PubMed: 19910922]
26. Banke TG, Traynelis SF. Activation of NR1/NR2B NMDA receptors. Nat Neurosci. 2003; 6:144–152. DOI: 10.1038/nn1000 [PubMed: 12524545]
27. Farina AN, et al. Separation of domain contacts is required for heterotetrameric assembly of functional NMDA receptors. J Neurosci. 2011; 31:3565–3579. DOI: 10.1523/JNEUROSCI.6041-10.2011 [PubMed: 21389213]
28. Jespersen A, Tajima N, Fernandez-Cuervo G, Garnier-Amblard EC, Furukawa H. Structural insights into competitive antagonism in NMDA receptors. Neuron. 2014; 81:366–378. DOI: 10.1016/j.neuron.2013.11.033 [PubMed: 24462099]
29. Vance KM, Simorowski N, Traynelis SF, Furukawa H. Ligand-specific deactivation time course of GluN1/GluN2D NMDA receptors. Nat Commun. 2011; 2:294. [PubMed: 21522138]
30. Durr KL, et al. Structure and Dynamics of AMPA Receptor GluA2 in Resting, Pre-Open, and Desensitized States. Cell. 2014; 158:778–792. DOI: 10.1016/j.cell.2014.07.023 [PubMed: 25109876]
31. Kazi R, Dai J, Sweeney C, Zhou HX, Wollmuth LP. Mechanical coupling maintains the fidelity of NMDA receptor-mediated currents. Nat Neurosci. 2014; 17:914–922. DOI: 10.1038/nn.3724 [PubMed: 24859202]
32. Popescu G, Auerbach A. The NMDA receptor gating machine: lessons from single channels. Neuroscientist. 2004; 10:192–198. DOI: 10.1177/1073858404263483 [PubMed: 15155058]
33. Popescu G, Robert A, Howe JR, Auerbach A. Reaction mechanism determines NMDA receptor response to repetitive stimulation. Nature. 2004; 430:790–793. DOI: 10.1038/nature02775 [PubMed: 15306812]
34. Otwinowski Z, Minor W. Processing of X-ray diffraction data collected in oscillation mode. Methods Enzymol. 1997; 276:307–326.
35. McCoy AJ, et al. Phaser crystallographic software. J Appl Crystallogr. 2007; 40:658–674. [PubMed: 19461840]
36. Adams PD, et al. PHENIX: building new software for automated crystallographic structure determination. Acta Crystallogr D Biol Crystallogr. 2002; 58:1948–1954. [PubMed: 12393927]
37. Grant T, Grigorieff N. Automatic estimation and correction of anisotropic magnification distortion in electron microscopes. J Struct Biol. 2015; 192:204–208. DOI: 10.1016/j.jsb.2015.08.006 [PubMed: 26278979]
38. Grant T, Grigorieff N. Measuring the optimal exposure for single particle cryo-EM using a 2.6 A reconstruction of rotavirus VP6. Elife. 2015; 4:e06980. [PubMed: 26023829]
39. Rohou A, Grigorieff N. CTFFIND4: Fast and accurate defocus estimation from electron micrographs. J Struct Biol. 2015; 192:216–221. DOI: 10.1016/j.jsb.2015.08.008 [PubMed: 26278980]
40. Lyumkis D, Brilot AF, Theobald DL, Grigorieff N. Likelihood-based classification of cryo-EM images using FREALIGN. J Struct Biol. 2013; 183:377–388. DOI: 10.1016/j.jsb.2013.07.005 [PubMed: 23872434]
41. Rosenthal PB, Henderson R. Optimal determination of particle orientation, absolute hand, and contrast loss in single-particle electron cryomicroscopy. J Mol Biol. 2003; 333:721–745. [PubMed: 14568533]
42. Pettersen EF, et al. UCSF Chimera--a visualization system for exploratory research and analysis. J Comput Chem. 2004; 25:1605–1612. DOI: 10.1002/jcc.20084 [PubMed: 15264254]
43. Emsley P, Lohkamp B, Scott WG, Cowtan K. Features and development of Coot. Acta Crystallogr D Biol Crystallogr. 2010; 66:486–501. DOI: 10.1107/S0907444910007493 [PubMed: 20383002]
44. Afonine PV, Headd JJ, Terwilliger TC, Adams PD. Computational Crystallography Newsletter. 2013; 4:43–44.

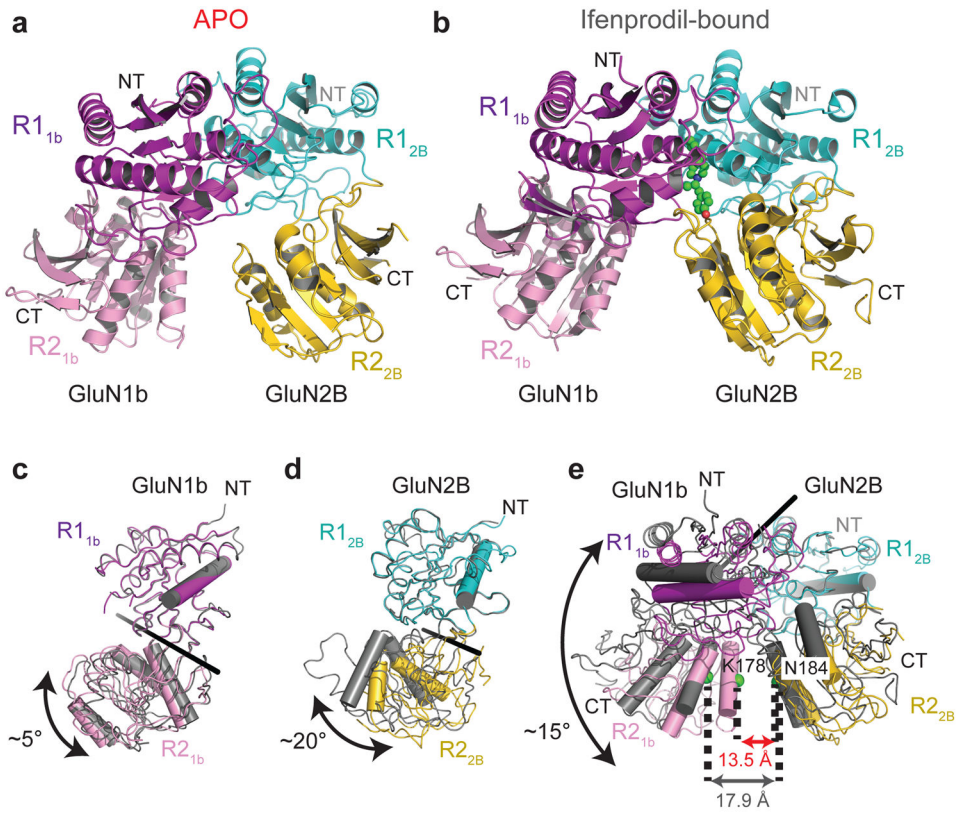

Figure 1. Structures of GluN1b-GluN2B ATD heterodimers

a,b, Crystal structure of the GluN1b-GluN2B ATD heterodimer in the apo state solved at 2.9 Å **(a)** in comparison with the ifenprodil-bound structure (PDB ID: 3QEL) **(b).** The R1 and R2 lobes are colored in magenta and light pink for GluN1b ATD and cyan and yellow for GluN2B ATD. Ifenprodil is represented with green spheres. **c,d,** Superposition of the R1 lobes of GluN1b **(c)** and GluN2B **(d)** in the apo- and ifenprodil-bound (grey) forms illustrates the relative 'opening' between R1 and R2 lobes. **e**, Superposing the GluN2B R1 lobes of apo- and ifenprodil-bound forms reveals ~15° rotation of GluN1b ATD relative to GluN2B ATD along the axis of rotation (black rod). The distance of the R2 lobes in the GluN1b-GluN2B heterodimers is measured between GluN1b Lys178 and GluN2B Asn184 (**b, e**; green spheres).

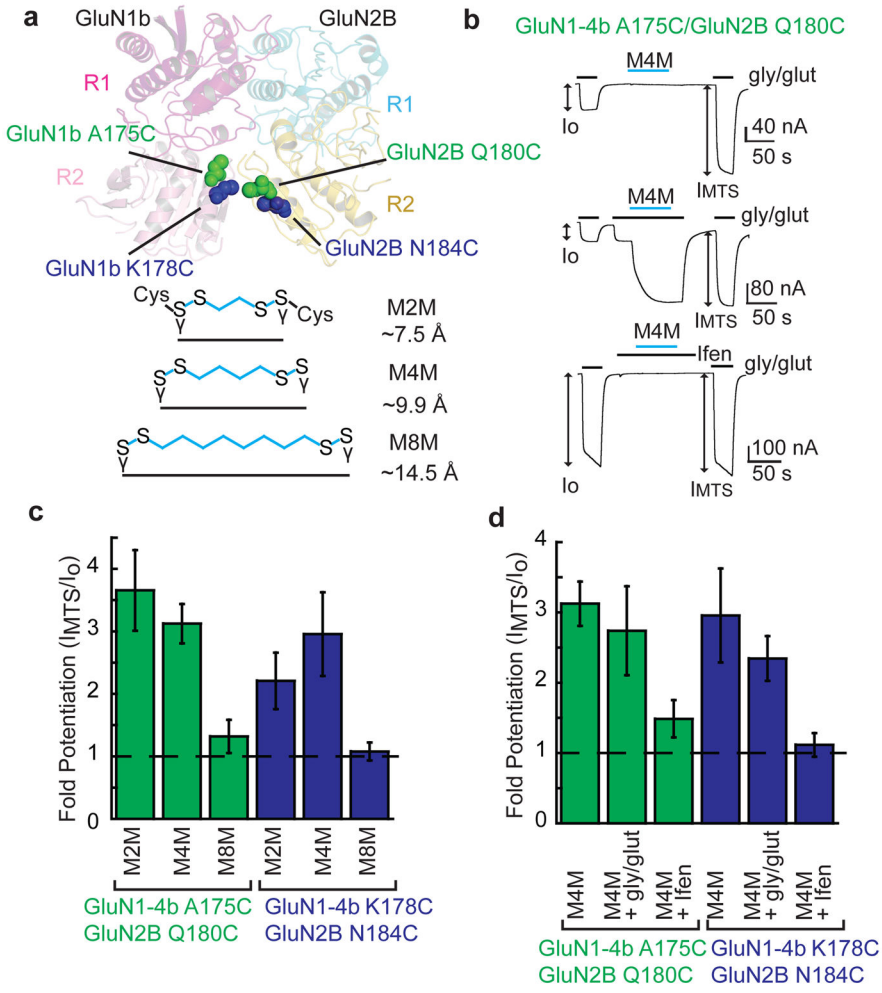

Figure 2. Conformational trap identifies the apo-GluN1b-GluN2B ATD structure as the "active" form

a, Location of engineered cysteines in the crystal structure of the apo-GluN1b-GluN2B ATD (GluN1-4b Ala175Cys/GluN2B Gln180Cys in green spheres and GluN1-4b Lys178Cys/GluN2B Asn184Cys in blue spheres). **b,** Application of 200 μM M4M in the presence or absence of 100 μM agonists (glycine (gly)/glutamate (glut)) potentiates the macroscopic current measured at the holding potential of −60 mV by TEVC. No potentiation was observed when M4M was applied in the presence of ifenprodil (Ifen). Shown here are the representative recording profiles for the GluN1-4b Ala175Cys/GluN2B Gln180Cys pair. **c–d**, 'Fold of potentiation' is presented as I_{MTS}/I_o as measured in panel b) for bifunctional MTS with different linker lengths **(c)** and M4M applied in different functional states **(d)**. Error bars represents ±s.d. for data obtained from at least five different oocytes ($n \geq 5$) per experiment.

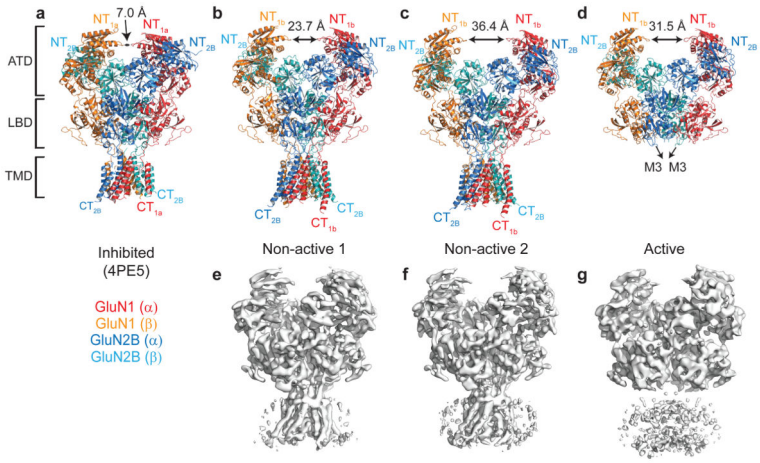

Figure 3. Overall structures of the intact GluN1-GluN2B NMDA receptors at different conformational states

a, The crystal structure of GluN1a-GluN2B NMDA receptor in complex with glycine, L-glutamate and ifenprodil (PDB ID: 4PE5). **b,c,d**, Cryo-EM structures of glycine and L-glutamate-bound GluN1b-GluN2B NMDA receptors classified to reveal different conformations representing the 'non-active' **(b,c)** and 'active' (**d**) states. The subunits are colored in red (GluN1 (α)), orange (GluN1 (β)), blue (GluN2B (α)) and cyan (GluN2B (β)). The two 'non-active' 3D classes (non-active 1 and 2) have difference distances between the two GluN1-GluN2B ATD heterodimers represented as the distance between Cαs of Glu 320 (299 in GluN1a) of GluN1b (α) and GluN1b (β) (double-sided arrows). The amino (NT) and carboxy (CT) termini and approximate domain boundaries are indicated by brackets. **e–g,** The cryo-EM maps for the 'non-active 1' **(e)**, 'non-active 2' **(f)**, and 'active' **(g)** states.

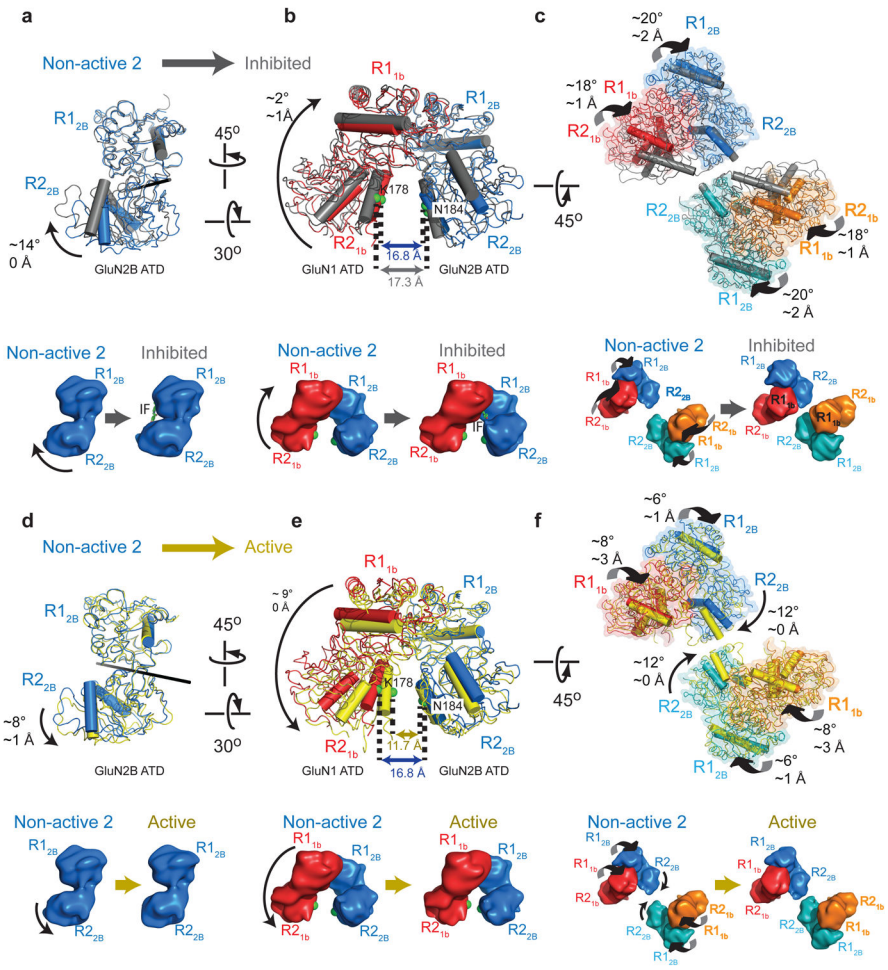

Figure 4. Changes in conformation and heterotetrameric subunit arrangement in ATD during ifenprodil inhibition and receptor activation

Comparison of 3D classes show movements (arrowed arcs) of the bi-lobed architecture in the GluN2B ATD **(a,d)**, and rearrangement of the GluN1b-GluN2B ATD heterodimer **(b,e)** and heterotetramer **(c,f)** during transition from the agonist-bound 'non-active 2' conformation (same color code as in Fig. 3) to the ifenprodil-bound 'inhibited' conformation (PDB ID: 4PE5) (grey) (**a–c**) or to the 'active' conformation (yellow) **(d–f)**. Schematic diagrams are shown below each panel. **a,d**, Superposition of GluN2B ATD R1 lobes show relative movement of R2 (around black rods) **(a,d)** and rearrangement in the pattern of subunit arrangement **(b,e)** in different functional states. **c**,**f**, GluN1b-GluN2B ATD heterotetramer from different 3D classes are compared by aligning the centers of masses (COMs) of the ATD heterotetramer, LBD heterotetramer and individual LBDs.

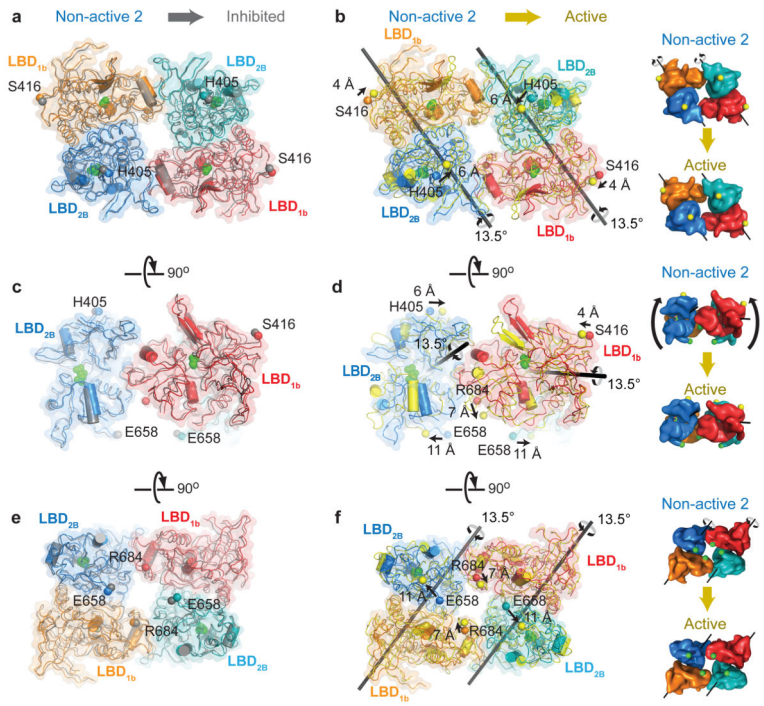

Figure 5. Conformational changes at the LBD during ifenprodil inhibition and receptor activation

The same superposition as in Fig. 4c,f viewing the LBD tetramers in the 'non-active 2' (same color code as in Fig. 3), the 'inhibited' (grey) (**a, c, e**) and the 'activate' (yellow) states **(b,d,f)** from ATD (**a,b**), side (**c,d**) and TMD (**e,f**). The LBD heterodimers rotates (around black rods) during transition from 'non-active 2' to 'active' while little or no change occurs between 'non-active 2' and 'inhibited.' Cα atoms of the residues at the ATD-LBD linker (GluN1b His 405 and GluN2B Ser 416) and the LBD-TMD linker (GluN1b Arg 684 and GluN2B Glu 658) are shown as yellow and green spheres, respectively. Glycine and L-glutamate at the cleft of the LBD bi-lobes are shown in green spheres. Schematic diagrams are shown to the right of each panel.

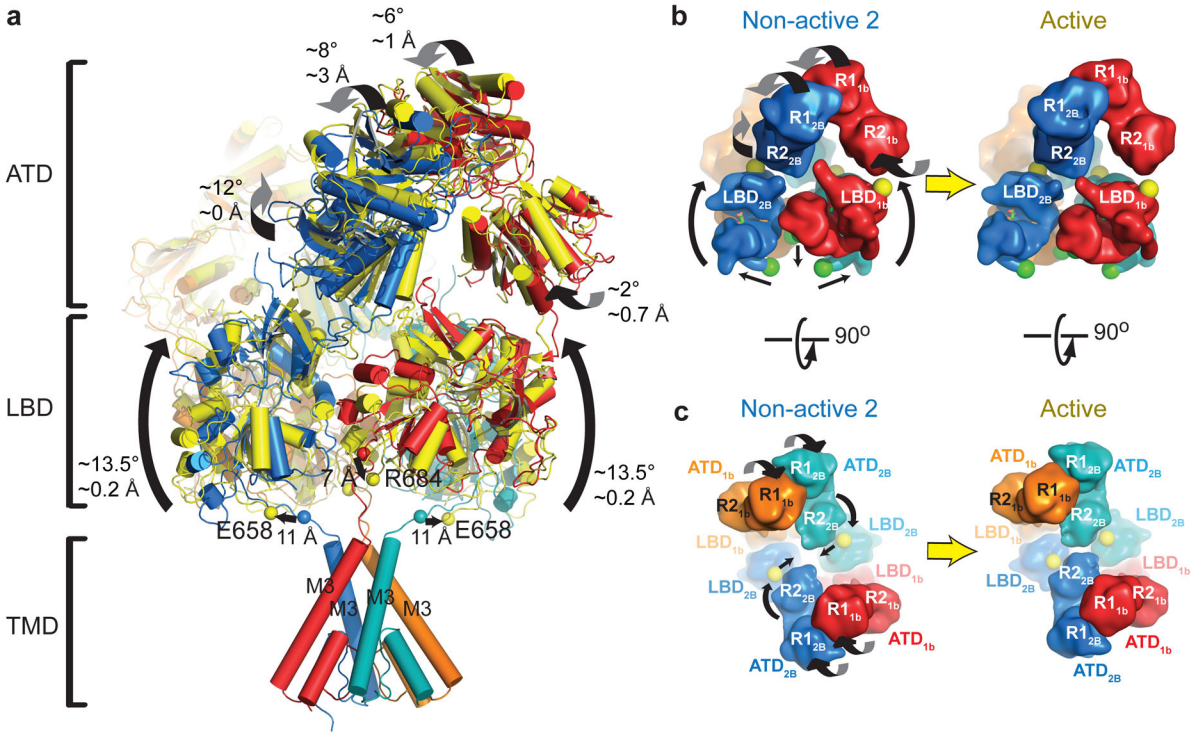

Figure 6. Consorted movement of the ATD and LBD opens the gate

a, Structural comparison of NMDA receptors in the ‘non-active 2’ (same color code as in Fig. 3) and the ‘active’ (yellow) conformations as in Fig. 4 and 5. The M1 and M4 helices of TMD are omitted for clarity. The arrowed arcs indicate rotation from ‘non-active 2’ to ‘active.’ The first ordered residues on the linker between the M3 helices on TMD and the LBD in the ‘active’ structure (GluN1b Arg 684 and GluN2B Glu 658) are shown as spheres. **b–c**, Schematic diagram viewed from the side of the tetramer (**b**) and top of the ATD (**c**). GluN1b Arg 684 and GluN2B Glu 658 are shown as green spheres and the residues at the ATD-LBD linker (GluN1b Ser 416 and GluN2B His 405) are shown as yellow spheres.